Curvature-enhanced spin-orbit coupling in a carbon nanotube

Jae-Seung Jeong and Hyun-Woo Lee
Department of Physics and PCTP, Pohang University of Science and Technology, Pohang 790-784, Korea
(Received 21 July 2009; published 7 August 2009)

Structure of the spin-orbit coupling varies from material to material and thus finding the correct spin-orbit coupling structure is an important step toward advanced spintronic applications. We show theoretically that the curvature in a carbon nanotube generates two types of the spin-orbit coupling, one of which was not recognized before. In addition to the topological phase-related contribution of the spin-orbit coupling, which appears in the off-diagonal part of the effective Dirac Hamiltonian of carbon nanotubes, there is another contribution that appears in the diagonal part. The existence of the diagonal term can modify spin-orbit coupling effects qualitatively, an example of which is the electron-hole asymmetric spin splitting observed recently, and generate four qualitatively different behavior of energy-level dependence on parallel magnetic field. It is demonstrated that the diagonal term applies to a curved graphene as well. This result should be valuable for spintronic applications of graphitic materials.

DOI: 10.1103/PhysRevB.80.075409 PACS number(s): 73.22.−f, 71.70.Ej

I. INTRODUCTION

Graphitic materials such as carbon nanotubes (CNTs) and graphenes are promising materials for spintronic applications. Various types of spintronic devices are reported such as CNT-based three-terminal magnetic tunnel junctions,[1] spin diodes,[2] and graphene-based spin valves.[3] Graphitic materials are believed to be excellent spin conductors.[4] The hyperfine interaction of electron spins with nuclear spins is strongly suppressed since ^{12}C atoms do not carry nuclear spins. It is estimated that the spin-relaxation time in a CNT (Ref. 5) and a graphene[6] is limited by the spin-orbit coupling (SOC).

Carbon atoms are subject to the atomic SOC Hamiltonian H_{so}. In an ideal flat graphene, the energy shift caused by H_{so} is predicted to be $\sim 10^{-3}$ meV.[7,8] Recently it is predicted[8,9] that the geometric curvature can enhance the effective strength of the SOC by orders of magnitude. This mechanism applies to a CNT and also to a graphene which, in many experimental situations, exhibits nanometer-scale corrugations.[10] There is also a suggestion[11] that artificial curved structures of a graphene may facilitate device applications.

A recent experiment[12] on ultraclean CNTs measured directly the energy shifts caused by the SOC, which provides an ideal opportunity to test theories of the curvature-enhanced SOC in graphitic materials. The measured shifts are in order-of-magnitude agreement with the theoretical predictions,[8,9] confirming that the curvature indeed enhances the effective SOC strength. The experiment revealed discrepancies as well while existing theories predict the same strength of the SOC for electrons and holes, which is natural considering that both the conduction and valence bands originate from the same π orbital, the experiment found considerable asymmetry in the SOC strength between electrons and holes. This electron-hole asymmetry implies that existing theories of the SOC in graphitic materials are incomplete.

In this paper, we show theoretically that in addition to effective SOC in the off-diagonal part of the effective Dirac Hamiltonian, which was reported in the existing theories,[8,9] there exists an additional type of the SOC that appears in the diagonal part both in CNTs and curved graphenes. It is demonstrated that the combined action of the two types of the SOC produces the electron-hole asymmetry observed in the CNT experiment[12] and gives rise to four qualitatively different behavior of energy-level dependence on magnetic field parallel to the CNT axis.

This paper is organized as follows. In Sec. II, we show analytical expressions of two types of the effective SOC in a CNT and then explain how the electron-hole asymmetric spin splitting can be generated in semiconducting CNTs generically. Section III describes the second-order perturbation theory that is used to calculate the effective SOC and summarizes the tight-binding models of the atomic SOC and geometric curvature. Section IV reports four distinct energy-level dependence on magnetic field parallel to the CNT axis. We conclude in Sec. V with implications of our theory on curved graphenes and a brief summary.

II. EFFECTIVE SPIN-ORBIT COUPLING IN A CNT

We begin our discussion by presenting the first main result for a CNT with the radius R and the chiral angle $\theta\,[0 \le \theta \le \pi/6,\ 0(\pi/6)$ for zigzag (armchair) CNTs]. We find that when the two sublattices A and B of the CNT are used as bases, the curvature-enhanced effective SOC Hamiltonian $\mathcal{H}_{\mathrm{soc}}$ near the K point with Bloch momentum $\mathbf{K}$ becomes

$$\mathcal{H}_{\mathrm{soc}}^{\mathrm{K}} = \begin{pmatrix} (\delta_{\mathrm{K}}'/R)\sigma_y & (\delta_{\mathrm{K}}/R)\sigma_y \\ (\delta_{\mathrm{K}}^{*}/R)\sigma_y & (\delta_{\mathrm{K}}'/R)\sigma_y \end{pmatrix}, \tag{1}$$

where σ_y represents the real spin Pauli matrix along the CNT axis. The pseudospin is defined to be up (down) when an electron is in the sublattice $A(B)$. Here the off-diagonal term that can be described by a spin-dependent topological phase are reported in Refs. 8 and 9 but the diagonal term was not recognized before. Expressions for the parameters δ_{K} and δ_{K}' are given by[13]

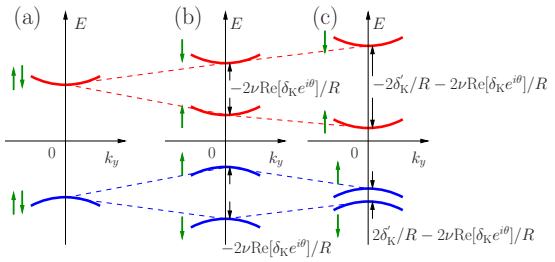

FIG. 1. (Color online) Schematic of the lowest conduction-band (red, $E>0$) and highest valence-band (blue, $E<0$) positions of a semiconducting CNT predicted by $\mathcal{H}^{\mathrm{K}}_{\mathrm{Dirac}}+\mathcal{H}^{\mathrm{K}}_{\mathrm{soc}}$ for (a) $\delta_{\mathrm{K}}=\delta'_{\mathrm{K}}=0$, (b) $\delta_{\mathrm{K}}\neq 0$, $\delta'_{\mathrm{K}}=0$, and (c) $\delta_{\mathrm{K}}\neq 0$, $\delta'_{\mathrm{K}}\neq 0$. In (c), the conduction or valence band has larger spin splitting depending on the sign of ν. Arrows (green) show the spin direction along the CNT. The expressions for the energy-level spacing are also provided. When they are negative, the positions of the two spin-split bands should be swapped.

$$\frac{\delta_{\mathrm{K}}}{R}=\frac{\lambda_{\mathrm{so}}a(\varepsilon_s-\varepsilon_p)(V^{\pi}_{pp}+V^{\sigma}_{pp})}{12\sqrt{3}V^{\sigma 2}_{sp}}\frac{e^{-i\theta}}{R} \tag{2}$$

and

$$\frac{\delta'_{\mathrm{K}}}{R}=\frac{\lambda_{\mathrm{so}}aV^{\pi}_{pp}}{2\sqrt{3}(V^{\sigma}_{pp}-V^{\pi}_{pp})}\frac{\cos 3\theta}{R}, \tag{3}$$

where $\lambda_{\mathrm{so}}\sim 12$ meV (Ref. 14) is the atomic SOC constant, a is the lattice constant 2.49 Å, and $\varepsilon_{s(p)}$ is the atomic energy for the $s(p)$ orbital. Here, V^{σ}_{sp} and $V^{\pi(\sigma)}_{pp}$ represent the coupling strengths in the absence of the curvature for the σ coupling between nearest-neighbor s and p orbitals and the $\pi(\sigma)$ coupling between nearest-neighbor p orbitals, respectively. Note that the $|\delta'_{\mathrm{K}}|$ has the θ dependence, whose implication on the CNT energy spectrum is addressed in Sec. IV. For K′ point with $\mathbf{K}'=-\mathbf{K}$, $\mathcal{H}^{\mathrm{K}'}_{\mathrm{soc}}$ is given by Eq. (1) with δ_{K} and δ'_{K} replaced by $\delta_{\mathrm{K}'}=-\delta^{*}_{\mathrm{K}}$ and $\delta'_{\mathrm{K}'}=-\delta'_{\mathrm{K}}$, respectively.

Implications of the diagonal term of the SOC become evident when Eq. (1) is combined with the two-dimensional Dirac Hamiltonian $\mathcal{H}_{\mathrm{Dirac}}$ of the CNT. For a state near the K point with the Bloch momentum $\mathbf{K}+\mathbf{k}$ [$\mathbf{k}=(k_x,k_y)$, $|\mathbf{k}|\ll|\mathbf{K}|$], $\mathcal{H}_{\mathrm{Dirac}}$ becomes[15]

$$\mathcal{H}^{\mathrm{K}}_{\mathrm{Dirac}}=\hbar v_{\mathrm{F}}\begin{pmatrix}0 & e^{-i\theta}(k_x-ik_y)\\ e^{+i\theta}(k_x+ik_y) & 0\end{pmatrix}, \tag{4}$$

where v_F is the Fermi velocity and the momentum component k_x along the circumference direction satisfies the quantization condition $k_x=(1/3R)\nu$ for a (n,m) CNT with $n-m=3q+\nu$ ($q\in\mathbb{Z}$ and $\nu=\pm 1,0$) and $\theta=\tan^{-1}[\sqrt{3}m/(2n+m)]$. For a semiconducting ($\nu=\pm 1$) CNT, the diagonalization of $\mathcal{H}^{\mathrm{K}}_{\mathrm{Dirac}}+\mathcal{H}^{\mathrm{K}}_{\mathrm{soc}}$ results in different spin splittings [Fig. 1(c)] of $-2\delta'_{\mathrm{K}}/R-2\nu\,\mathrm{Re}[\delta_{\mathrm{K}}e^{i\theta}]/R$ and $2\delta'_{\mathrm{K}}/R-2\nu\,\mathrm{Re}[\delta_{\mathrm{K}}e^{i\theta}]/R$ for the conduction and valence bands, respectively. This explains the electron-hole asymmetry observed in the recent experiment.[12] Here we remark that neither the off-diagonal (δ_{K}) nor the diagonal (δ'_{K}) term of the SOC alone can generate the electron-hole asymmetry since the two spin splittings can differ by sign at best, which actually implies the same magnitude of the spin splitting (see Fig. 1 for the sign convention). Thus the interplay of the two types is crucial for the asymmetry.

III. THEORY AND MODEL

We calculate the δ_{K} and δ'_{K} analytically using degenerate second-order perturbation theory and treating atomic SOC and geometric curvature as perturbation. For simplicity, we evaluate δ_{K} and δ'_{K} in the limit $\mathbf{k}=0$. Although this limit is not strictly valid since $\mathbf{k}=0$ does not generally satisfy the quantization condition on k_x, one may still take this limit since the dependence of δ_{K} and δ'_{K} on $\mathbf{k}$ is weak. An electron at the K point is described by the total Hamiltonian $H^{\mathrm{K},(0)}+H_{\mathrm{so}}+H_{\mathrm{c}}$, where H_{c} describes the curvature effects and $H^{\mathrm{K},(0)}$ describes the π and σ bands in the absence of both H_{so} and H_{c}. The π-band eigenstates of $H^{\mathrm{K},(0)}$ are given by

$$|\Psi^{\mathrm{K},(0)}_{\uparrow(\downarrow)}\rangle=\frac{1}{\sqrt{2}}(\nu e^{-i\theta}|\psi^{\mathrm{K}}_A\rangle\pm|\psi^{\mathrm{K}}_B\rangle)\chi_{\uparrow(\downarrow)} \tag{5}$$

with the corresponding eigenvalues $E^{\mathrm{K},(0)}_{\uparrow(\downarrow)}\equiv E^{(0)}=0$. Here $|\Psi^{\mathrm{K},(0)}_{\uparrow(\downarrow)}\rangle$ with the upper (lower) sign amounts to the $\mathbf{k}=0$ limit of the eigenstate at the conduction-band bottom (valence-band top). $\chi_{\uparrow(\downarrow)}$ denotes the eigenspinor of σ_y. $|\psi^{\mathrm{K}}_{A(B)}\rangle=\frac{1}{\sqrt{N}}\sum_{r=\mathbf{r}_{A(B)}}e^{i\mathbf{K}\cdot r}|p^r_z\rangle$ is the orbital projection of $|\Psi^{\mathrm{K},(0)}_{\uparrow(\downarrow)}\rangle$ into the sublattice $A(B)$, $|p^r_z\rangle$ represents the p_z orbital at the atomic position r, and the z axis is perpendicular to the CNT surface.

When H_{so} and H_{c} are treated as weak perturbations, the first-order contribution H_{so} to the effective SOC vanishes since it causes the interband transition (Fig. 3) to the σ band.[8] The next leading-order contribution to the effective SOC comes from the following second-order perturbation Hamiltonian $H^{\mathrm{K},(2)}$ (Ref. 16):

$$H^{\mathrm{K},(2)}=H_{\mathrm{c}}\frac{\mathcal{P}^{\mathrm{K}}}{E^{(0)}-H^{\mathrm{K},(0)}}H_{\mathrm{so}}+\mathrm{H.c.}, \tag{6}$$

where the projection operator $\mathcal{P}^{\mathrm{K}}$ is defined by $\mathcal{P}^{\mathrm{K}}\equiv 1-\sum_{\alpha=\uparrow,\downarrow}|\Psi^{\mathrm{K},(0)}_{\alpha}\rangle\langle\Psi^{\mathrm{K},(0)}_{\alpha}|$. Another spin-dependent second-order term $H_{\mathrm{so}}[\mathcal{P}^{\mathrm{K}}/(E^{(0)}-H^{\mathrm{K},(0)})]H_{\mathrm{so}}$ (Ref. 17) is smaller than Eq. (6) (by two orders of magnitude for a CNT with $R\sim 2.5$ nm) and thus ignored. Then the second-order energy shift $E^{\mathrm{K},(2)}_{\uparrow(\downarrow)}$ is given by[18]

$$E^{\mathrm{K},(2)}_{\uparrow}=\langle\psi^{\mathrm{K}}_A|H^{\mathrm{K},(2)}|\psi^{\mathrm{K}}_A\rangle\pm\nu\,\mathrm{Re}[\langle\psi^{\mathrm{K}}_A|H^{\mathrm{K},(2)}|\psi^{\mathrm{K}}_B\rangle e^{i\theta}],$$

$$E^{\mathrm{K},(2)}_{\downarrow}=-E^{\mathrm{K},(2)}_{\uparrow}, \tag{7}$$

where the upper (lower) sign applies to the energy shift of the conduction-band bottom (valence-band top) and $\langle\psi^{\mathrm{K}}_A|H^{\mathrm{K},(2)}|\psi^{\mathrm{K}}_A\rangle=\langle\psi^{\mathrm{K}}_B|H^{\mathrm{K},(2)}|\psi^{\mathrm{K}}_B\rangle$ is used. Then by comparing $E^{\mathrm{K},(2)}_{\uparrow(\downarrow)}$ with Fig. 1, one finds

$$\frac{\delta_{\mathrm{K}}}{R}=\langle\psi^{\mathrm{K}}_A|H^{\mathrm{K},(2)}|\psi^{\mathrm{K}}_B\rangle,\quad \frac{\delta'_{\mathrm{K}}}{R}=\langle\psi^{\mathrm{K}}_A|H^{\mathrm{K},(2)}|\psi^{\mathrm{K}}_A\rangle. \tag{8}$$

Note that δ_{K} and δ'_{K} are related to pseudospin-flipping and pseudospin-conserving processes, respectively.

To evaluate Eq. (8), one needs explicit expressions for H_{so}, H_{c}, and $H^{\mathrm{K},(0)}$. H_{so} is given by $\lambda_{\mathrm{so}}\Sigma_r\mathbf{L}_r\cdot\mathbf{S}_r$,[7] where $\mathbf{L}_r$

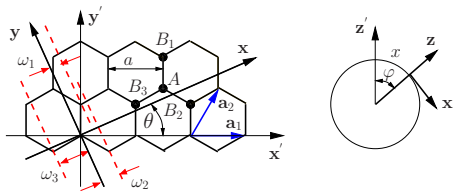

FIG. 2. (Color online) Two-dimensional honeycomb lattice structure. $\mathbf{x}(\mathbf{y})$ is the coordinate around (along) the CNT with chiral vector $n\mathbf{a}_1+m\mathbf{a}_2\equiv(n,m)$ and chiral angle θ. $\omega_j(j=1,2,3)$, the length between y axis passing A atom and its parallel (red dashed) line is related with ξ_j by $\xi_j\approx\omega_j/(2R)$ [Eq. (10)]. The coordinates for the CNT is illustrated on the right. Here, $x=\varphi R$.

and $\mathbf{S}_r$ are, respectively, the atomic-orbital and spin angular momentum of an electron at a carbon atom r. The tight-binding Hamiltonian of the H_{so} can be written[8] as $H_{so}=(\lambda_{so}/2)\Sigma_{r=\mathbf{r}_{A/B}}(c^{z\dagger}_{r-}c^{x}_{r+}-c^{z\dagger}_{r+}c^{x}_{r-}+ic^{z\dagger}_{r+}c^{y}_{r-}+ic^{z\dagger}_{r-}c^{y}_{r+}+ic^{y\dagger}_{r+}c^{x}_{r+}-ic^{y\dagger}_{r-}c^{x}_{r-})+\text{H.c.}$, where $c^{x}_{r+(-)}$, $c^{y}_{r+(-)}$, and $c^{z}_{r+(-)}$ denote the annihilation operators for $|p^{r}_{x}\rangle\chi_{+(-)}$, $|p^{r}_{y}\rangle\chi_{+(-)}$, and $|p^{r}_{z}\rangle\chi_{+(-)}$. Here $\chi_{+(-)}$ denotes the eigenspinor of σ_z (+/− for outward/inward). For later convenience, we express $\chi_{+(-)}$ in term of $\chi_{\uparrow(\downarrow)}$ to obtain a expression for H_{so},

$$H_{so}=\frac{\lambda_{so}}{2}\sum_{r=\mathbf{r}_{A/B}}[i(c^{z\dagger}_{r\downarrow}c^{x}_{r\downarrow}-c^{z\dagger}_{r\uparrow}c^{x}_{r\uparrow})+(e^{-i\varphi}c^{z\dagger}_{r\uparrow}c^{y}_{r\downarrow}-e^{i\varphi}c^{z\dagger}_{r\downarrow}c^{y}_{r\uparrow})+i(e^{-i\varphi}c^{y\dagger}_{r\uparrow}c^{x}_{r\downarrow}+e^{i\varphi}c^{y\dagger}_{r\downarrow}c^{x}_{r\uparrow})]+\text{H.c.} \quad (9)$$

For the curvature Hamiltonian H_c, we retain only the leading-order term in the expansion in terms of a/R. Up to the first order in a/R, H_c reduces to $H_c^{\pi\sigma}$,

$$H_c^{\pi\sigma}=\sum_{\mathbf{r}_A}\sum_{j=1}^{3}\sum_{\alpha=\uparrow,\downarrow}[S_j(c^{z\dagger}_{\mathbf{r}_A\alpha}c^{s}_{B_j\alpha}+c^{s\dagger}_{\mathbf{r}_A\alpha}c^{z}_{B_j\alpha})+X_j(c^{z\dagger}_{\mathbf{r}_A\alpha}c^{x}_{B_j\alpha}-c^{x\dagger}_{\mathbf{r}_A\alpha}c^{z}_{B_j\alpha})+Y_j(c^{z\dagger}_{\mathbf{r}_A\alpha}c^{y}_{B_j\alpha}-c^{y\dagger}_{\mathbf{r}_A\alpha}c^{z}_{B_j\alpha})]+\text{H.c.}, \quad (10)$$

where $\mathbf{r}_A$ is a lattice site in the sublattice A and its three nearest-neighbor sites in the sublattice B are represented by B_j $(j=1,2,3)$ (Fig. 2). Here S_j, X_j, and Y_j are proportional to a/R and denote the curvature-induced coupling strengths of s, p_x, and p_y orbitals with a nearest-neighbor p_z orbital. Their precise expressions that can be determined purely from geometric considerations, are given by $S_j=\xi_j\tilde{S}_j$, $X_j=\xi_j\tilde{X}_j$, and $Y_j=\xi_j\tilde{Y}_j$ with $\xi_1\approx a/(2\sqrt{3}R)\sin\theta$, $\xi_2\approx a/(2\sqrt{3}R)\sin(\pi/3-\theta)$, and $\xi_3\approx a/(2\sqrt{3}R)\sin(\pi/3+\theta)$ (Fig. 2). Here

$$\tilde{S}_1=V^{\sigma}_{sp}\sin\theta,$$

$$\tilde{S}_2=V^{\sigma}_{sp}\cos\left(\frac{\pi}{6}+\theta\right),$$

$$\tilde{S}_3=V^{\sigma}_{sp}\cos\left(\frac{\pi}{6}-\theta\right),$$

$$\tilde{X}_1=-V^{\sigma}_{pp}\sin^2\theta-V^{\pi}_{pp}-V^{\pi}_{pp}\cos^2\theta,$$

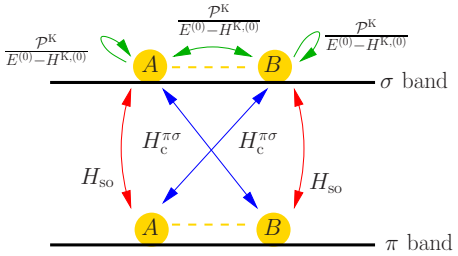

FIG. 3. (Color online) Schematic of the second-order transition process generated by $H^{K,(2)}$ [Eq. (6)]. Pseudospin transitions (between the sublattices A and B) and interband transitions (between π and σ bands) are illustrated.

$$\tilde{X}_2=-V^{\sigma}_{pp}\sin^2\left(\frac{\pi}{3}-\theta\right)-V^{\pi}_{pp}-V^{\pi}_{pp}\cos^2\left(\frac{\pi}{3}-\theta\right),$$

$$\tilde{X}_3=V^{\sigma}_{pp}\sin^2\left(\frac{\pi}{6}-\theta\right)+V^{\pi}_{pp}+V^{\pi}_{pp}\cos^2\left(\frac{\pi}{6}-\theta\right),$$

$$\tilde{Y}_1=\sin(2\theta)\frac{V^{\pi}_{pp}-V^{\sigma}_{pp}}{2},$$

$$\tilde{Y}_2=\sin\left(2\theta-\frac{2\pi}{3}\right)\frac{V^{\pi}_{pp}-V^{\sigma}_{pp}}{2},$$

$$\tilde{Y}_3=\sin\left(2\theta-\frac{\pi}{3}\right)\frac{V^{\pi}_{pp}-V^{\sigma}_{pp}}{2}. \quad (11)$$

Lastly, for the factor $H^{K,(0)}$, we use the Slater-Koster parametrization[19] for nearest-neighbor hopping. In σ-band calculation, s, p_x, and p_y orbitals are used as basis.

Combined effects of the three factors H_{so}, $\mathcal{P}^K/(E^{(0)}-H^{K,(0)})$, and H_c are illustrated in Fig. 3. The real spin dependence arises solely from H_{so}, which generates the factor σ_y.[20] For the pseudospin, the combined effect of H_{so} and H_c is to flip the pseudospin. When they are combined with the pseudospin-conserving part of $\mathcal{P}^K/(E^{(0)}-H^{K,(0)})$, one obtains the pseudospin-flipping process [Eq. (8)] determining δ_K. In addition, $\mathcal{P}^K/(E^{(0)}-H^{K,(0)})$ contains the pseudospin-flipping part, which is natural since states localized in one particular sublattice are not eigenstates of $H^{K,(0)}$. When the pseudospin-flipping part of $\mathcal{P}^K/(E^{(0)}-H^{K,(0)})$ is combined with H_{so} and H_c, one obtains the pseudospin-conserving process [Eq. (8)] determining δ'_K.

The signs of $\delta_K e^{i\theta}$ and $\delta'_K/\cos 3\theta$ are negative. We find $|(\delta'_K/\cos 3\theta)/\delta_K|=4.5$ for tight-binding parameters in Ref. 21. Thus δ'_K is of the same order as δ_K,[22] which is understandable since pseudospin-flipping terms in $E^{(0)}-H^{K,(0)}$ (with amplitudes V^{σ}_{pp} and V^{σ}_{sp}) are comparable in magnitude to pseudospin-conserving terms (with amplitudes $E^{(0)}-\varepsilon_{s(p)}$).

IV. BEHAVIOR IN A MAGNETIC FIELD

Next we examine further implications of our result in view of the experiment,[12] where the conduction-band bottom and valence-band top positions of semiconducting CNTs

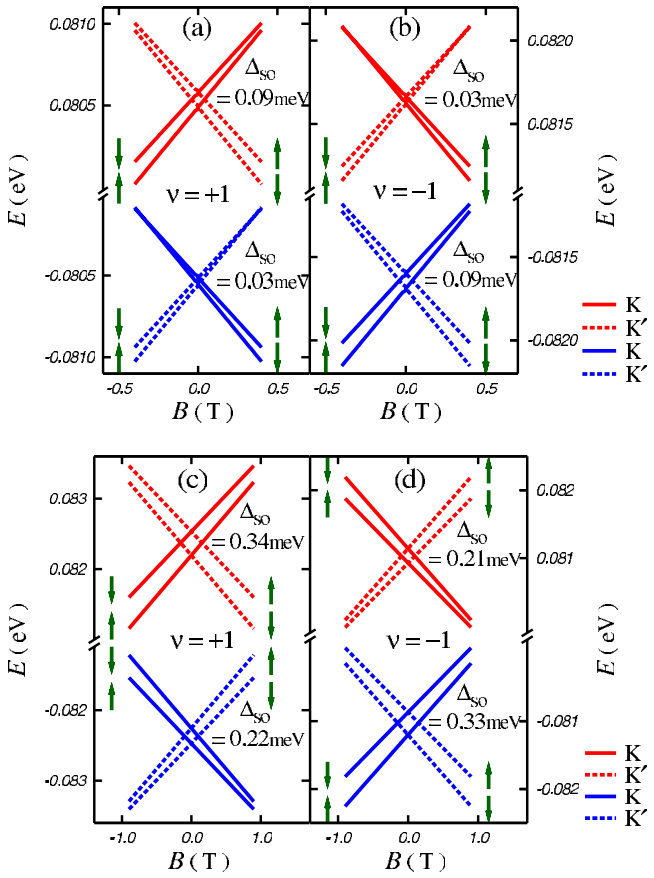

FIG. 4. (Color online) Calculated energy spectrum of the conduction-band bottom (red, $E>0$) and valence-band top (blue, $E<0$) near K (solid lines) and K′ (dashed lines) points in semiconducting CNTs with $R\approx 2.5$ nm as a function of magnetic field B parallel to the CNT axis. The chiral vectors for each CNT are (a) (38,34), (b) (39,34), (c) (61,0), and (d) (62,0), respectively. Arrows (green) show spin direction along the CNT axis and Δ_{so} denotes the zero-field splitting. Assuming $k_y=0$, the energy E including the SOC, the Aharonov-Bohm flux (Ref. 15) $\phi_{AB}=B\pi R^2$, and the Zeeman coupling effects is, $E=\pm\hbar v_F\sqrt{[k_x+(1/R)(\phi_{AB}/\phi_0)]^2+E_{\uparrow(\downarrow)}^{K(K'),(2)}}+(g/2)\mu_B\tau_\parallel B$, with upper (lower) sign applying to the conduction (valence) band. $\phi_0=hc/|e|$, $\tau_\parallel=+1(-1)$ for $\chi_{\uparrow(\downarrow)}$, $v_F=-aV_{pp}^{\pi}\sqrt{3}/2$, and $g=2$ (Ref. 12). For estimation of $E_{\uparrow(\downarrow)}^{K(K'),(2)}$, we use tight-binding parameters in Ref. 21; $V_{ss}^{\sigma}=-4.76$ eV, $V_{sp}^{\sigma}=4.33$ eV, $V_{pp}^{\sigma}=4.37$ eV, $V_{pp}^{\pi}=-2.77$ eV, $\varepsilon_s=-6.0$ eV, and $\varepsilon_p=0$ (Ref. 22).

($\nu=\pm 1$) are measured as a function of the magnetic field B parallel to the CNT axis. We find that the θ dependence [Eq. (3)] of δ_K' has interesting implications. When $\cos 3\theta$ is sufficiently close to 0 (close to armchair-type), $|\delta_K'|$ is smaller than $|\delta_K e^{i\theta}|$. The prediction of our theory in this situation is shown in Figs. 4(a) and 4(b). Note that the spin splitting of both the conduction and valence bands becomes smaller as the energy E increases. On the other hand, when $\cos 3\theta$ is sufficiently close to 1 (close to zigzag-type), $|\delta_K'|$ is larger than $|\delta_K e^{i\theta}|$. In this situation [Figs. 4(c) and 4(d)], the energy dependence of either valence or conduction band is inverted; for $\nu=+1(-1)$, the spin splitting of the valence (conduction) band becomes *larger* as the energy increases.

Combined with the electron-prevailing [Figs. 4(a) and 4(c) for $\nu=+1$] vs hole-prevailing [Figs. 4(b) and 4(d) for $\nu=-1$] asymmetries in the zero-field splitting, one then finds that there exist four distinct patterns of E vs B diagram, which is the second main result of this paper. Among these four patterns, only the pattern in Fig. 4(a) is observed in the experiment,[12] which measured two CNT samples. We propose further experiments to test the existence of the other three patterns.

Here we remark that although Eqs. (1)–(3) are demonstrated so far for semiconducting CNTs, they hold for metallic CNTs ($\nu=0$) as well. For armchair CNTs with $\cos 3\theta=0$, δ_K' becomes zero and the spin splitting is determined purely by δ_K. For metallic but nonarmchair CNTs, finding implications of Eq. (1) is somewhat technical since the curvature-induced minigap appears near the Fermi level.[23] Our calculation for (37,34)($\cos 3\theta\approx 0$) and (60,0)($\cos 3\theta=1$) CNTs including the minigap effect indicates that they show behaviors similar to Figs. 4(b) and 4(d), respectively. Thus nominally metallic CNTs exhibit spin-splitting patterns of $\nu=-1$ CNTs.

V. DISCUSSION AND SUMMARY

Lastly we discuss briefly the effective SOC in a curved graphene.[10] Unlike CNTs, there can be both convex-shaped and concave-shaped curvatures in a graphene. We first address the convex-shaped curvatures. When the local structure of a curved graphene has two principal curvatures, $1/R_1$ and $1/R_2$ with the corresponding binormal unit vectors $\mathbf{n}_1$ and $\mathbf{n}_2$, each principal curvature $1/R_i$ ($i=1,2$) generates the effective SOC, Eq. (1), with σ_y replaced by $\boldsymbol{\sigma}\cdot\mathbf{n}_i$ and R by R_i. The corresponding δ_i and δ_i' values are given by Eqs. (2) and (3) with θ replaced by θ_i, where θ_i is the chiral angle with respect to $\mathbf{n}_i$. Thus the diagonal term of the effective SOC is again comparable in magnitude to the off-diagonal term. For the concave-shaped curvatures, we find that the two types of the SOC become $-\delta_i$ and $-\delta_i'$ with θ_i, respectively. We expect that this result may be relevant for the estimation of the spin-relaxation length in graphenes[6] and may provide insights into unexplained experimental data in graphene-based spintronic systems.[24] We also remark that the effective SOC in a graphene may be spatially inhomogeneous since the local curvature of the nanometer-scale corrugations[10] is not homogeneous, whose implications go beyond the scope of this paper.

In summary, we have demonstrated that the interplay of the atomic SOC and the curvature generates two types of the effective SOC in a CNT, one of which was not recognized before. Combined effects of the two types of the SOC in CNTs explain recently observed electron-hole asymmetric spin splitting[12] and generates four qualitatively different types of energy-level dependence on the parallel magnetic field. Our result may have interesting implications for graphenes as well.

Note added. While we were preparing our manuscript, we became aware of a related paper.[25] However the effective Hamiltonian [Eq. (1)] for the SOC and the four distinct types of the magnetic field dependence (Fig. 4) are not reported in the work.

ACKNOWLEDGMENTS

We appreciate Philp Kim for his comment for the curved graphenes. We acknowledge the hospitality of Hyunsoo Yang and Young Jun Shin at National University of Singapore, where parts of this work were performed. We thank Seung-Hoon Jhi, Woojoo Sim, Seon-Myeong Choi, and Dong-Keun Ki for helpful conversations. This work was supported by the KOSEF (Basic Research Program No. R01-2007-000-20281-0) and BK21.

[1] S. Sahoo, T. Kontos, J. Furer, C. Hoffmann, M. Gräber, A. Cuttet, and C. Schönenberger, Nat. Phys. **1**, 99 (2005).

[2] C. A. Merchant and N. Marković, Phys. Rev. Lett. **100**, 156601 (2008).

[3] N. Tombros, C. Jozsa, M. Popinciuc, H. T. Jonkman, and B. J. van Wees, Nature (London) **448**, 571 (2007); S. Cho, Y.-F. Chen, and M. S. Fuhrer, Appl. Phys. Lett. **91**, 123105 (2007).

[4] K. Tsukagoshi, B. W. Alphenaar, and H. Ago, Nature (London) **401**, 572 (1999).

[5] D. V. Bulaev, B. Trauzettel, and D. Loss, Phys. Rev. B **77**, 235301 (2008).

[6] D. Huertas-Hernando, F. Guinea, and A. Brataas, arXiv:0812.1921 (unpublished).

[7] H. Min, J. E. Hill, N. A. Sinitsyn, B. R. Sahu, L. Kleinman, and A. H. MacDonald, Phys. Rev. B **74**, 165310 (2006); Y. Yao, F. Ye, X.-L. Qi, S.-C. Zhang, and Z. Fang, *ibid.* **75**, 041401(R) (2007).

[8] D. Huertas-Hernando, F. Guinea, and A. Brataas, Phys. Rev. B **74**, 155426 (2006).

[9] T. Ando, J. Phys. Soc. Jpn. **69**, 1757 (2000); A. DeMartino, R. Egger, K. Hallberg, and C. A. Balseiro, Phys. Rev. Lett. **88**, 206402 (2002).

[10] J. C. Meyer, A. K. Geim, M. I. Katsnelson, K. S. Novoselov, T. J. Booth, and S. Roth, Nature (London) **446**, 60 (2007); E. Stolyarova, K. T. Rim, S. Ryu, J. Maultzsch, P. Kim, L. E. Brus, T. F. Heinz, M. S. Hybertsen, and G. W. Flynn, Proc. Natl. Acad. Sci. U.S.A. **104**, 9209 (2007); V. Geringer, M. Liebmann, T. Echtermeyer, S. Runte, M. Schmidt, R. Rückamp, M. C. Lemme, and M. Morgenstern, Phys. Rev. Lett. **102**, 076102 (2009); A. K. Geim, Science **324**, 1530 (2009).

[11] V. M. Pereira and A. H. Castro Neto, Phys. Rev. Lett. **103**, 046801 (2009).

[12] F. Kuemmeth, S. Ilani, D. C. Ralph, and P. L. McEuen, Nature (London) **452**, 448 (2008).

[13] The corresponding expression in Ref. 8 is slightly different from Eq. (2) since the σ band is treated in different ways. When a few minor mistakes in Ref. 8 are corrected, the two expressions result in similar numerical values.

[14] J. Serrano, M. Cardona, and T. Ruf, Solid State Commun. **113**, 411 (2000).

[15] J. Ajiki and T. Ando, J. Phys. Soc. Jpn. **62**, 1255 (1993).

[16] Leonard I. Schiff, *Quantum Mechanics* (McGraw-Hill, New York, 1968).

[17] $H_c[\mathcal{P}^K/(E^{(0)}-H^{K,(0)})]H_c$ is spin independent and thus ignored [see Eq. (10)].

[18] For the K′ point, $E_\uparrow^{K',(2)}=\langle\psi_A^{K'}|H^{K',(2)}|\psi_A^{K'}\rangle \pm \nu\,\mathrm{Re}[\langle\psi_A^{K'}|H^{K',(2)}|\psi_B^{K'}\rangle e^{-i\theta}]$, $E_\downarrow^{K',(2)}=-E_\uparrow^{K',(2)}$ with upper (lower) sign for the conduction-band bottom (valence-band top).

[19] J. C. Slater and G. F. Koster, Phys. Rev. **94**, 1498 (1954).

[20] The last four terms of H_{so} in Eq. (9), which do not commute with σ_y, do not contribute to the effective SOC near the Fermi energy due to the factor $e^{\pm i\varphi 8}$.

[21] J. W. Mintmire and C. T. White, Carbon **33**, 893 (1995).

[22] Using other sets of tight-binding parameters [D. Tománek and M. A. Schluter, Phys. Rev. Lett. **67**, 2331 (1991)]; [R. Saito, M. Fujita, G. Dresselhaus, and M. S. Dresselhaus, Phys. Rev. B **46**, 1804 (1992)] does not change results qualitatively.

[23] C. L. Kane and E. J. Mele, Phys. Rev. Lett. **78**, 1932 (1997); L. Yang and J. Han, *ibid.* **85**, 154 (2000); A. Kleiner and S. Eggert, Phys. Rev. B **63**, 073408 (2001); J.-C. Charlier, X. Blase, and S. Roche, Rev. Mod. Phys. **79**, 677 (2007).

[24] See, for instance, W. Han, W. H. Wang, K. Pi, K. M. McCreary, W. Bao, Y. Li, F. Miao, C. N. Lau, and R. K. Kawakami, Phys. Rev. Lett. **102**, 137205 (2009).

[25] L. Chico, M. P. López-Sancho, and M. C. Muñoz, Phys. Rev. B **79**, 235423 (2009).